ELSEVIER

Journal of Fluids and Structures 24 (2008) 1058–1076

JOURNAL OF FLUIDS AND STRUCTURES

www.elsevier.com/locate/jfs

Evaluation of Reynolds number effects on flutter derivatives of a flat plate by means of a computational approach

L. Bruno[a], D. Fransos[b,*]

[a]*Politecnico di Torino, Department of Structural Engineering and Geotechnics, Viale Mattioli 39, I-10125 Torino, Italy*
[b]*Politecnico di Torino, Department of Mathematics, C.so Duca degli Abruzzi 24, I-10129 Torino, Italy*

Received 9 April 2007; accepted 3 March 2008
Available online 7 May 2008

Abstract

This paper proposes an efficient method to determine the flutter derivatives of two-dimensional streamlined cylinders by means of a modified indicial approach adapted to a Navier–Stokes solver using an Arbitrary Lagrangian Eulerian formulation. The method relies on heave or pitch motion imposed on the structure according to smoothed-ramp-time histories and on the computational evaluation of the transient forces that arise on the obstacle. Hence, the indicial transfer function that relates the structural motion to the induced force in the frequency domain is obtained. The approach is applied to a flat plate of finite thickness and length immersed in a viscous flow. The low computational costs of the method allow the effects of Reynolds number to be evaluated on both the aerodynamic and aeroelastic behaviour for a wide range of Re values. The flow around the motionless plate is compared to the well-known Blasius and Goldstein solutions. The flutter derivatives extracted from simulations with a moving plate are compared to ones obtained from the Theodorsen function in the frame of the thin airfoil theory. Relationships between the variation of Re, the fluid flow phenomena and the flutter derivatives are highlighted in order to identify the flow field features that affect the flutter derivatives to the greatest extent.

Keywords: Computational wind engineering; Flutter derivatives; Indicial approach; Grid-based methods; Reynolds number effects

1. Introduction

The study of flutter instability of linelike, flexible structures is usually simplified by considering the two-dimensional (2-D) airflow around a representative rigid section along the main span of the structure. The relationship between the aeroelastic force on the section, induced by its own motion, and the motion itself can be expressed as an aeroelastic system that is characterized by transfer functions in the time or frequency domain between the input (motion) and output (force). It is worth pointing out that this approach leads to the formulation of a linear type aeroelastic system. The above-mentioned transfer functions have been expressed in this common modelling framework in different ways that depend on the application of interest. As for the time domain, the indicial approach was successfully used by Wagner (Fung, 1993) to give a closed-form solution of the transient lift evolution versus time (the so-called Wagner indicial lift function) of a 2-D flat thin plate placed in a potential flow and subjected to a step-wise pitch motion. As for

*Corresponding author. Tel.: +39 011 090 7558; fax: +39 011 090 7599.
E-mail address: davide.fransos@polito.it (D. Fransos).

0889-9746/$ - see front matter © 2008 Elsevier Ltd. All rights reserved.
doi:10.1016/j.jfluidstructs.2008.03.001

the frequency domain, the complex Theodorsen function was obtained by Theodorsen (1935) in analytical form by imposing a sinusoidal motion to the theoretical flat plate in the same flow conditions, that are well able to approximate the usual flying ones. Garrick (1938) demonstrated that the Theodorsen circulation function can be related to the Wagner indicial function by the Fourier transform. Theodorsen's modelling framework was first extended to bluff bodies moving in a viscous flow at moderate Reynolds numbers by Scanlan and Tomko (1971) who introduced frequency-dependent, empirical coefficients in place of the Theodorsen function, under the assumption that the linearity of the system still holds. Simiu and Scanlan (1996) related the resulting so-called flutter derivatives to the Theodorsen function in closed form, referring to the streamlined flat plate in a potential flow. To the authors' knowledge, the first attempt to evaluate the Reynolds number effects on the flutter derivatives of a symmetrical airfoil was made by Halfman (1952) and then more recently by Le-Maître et al. (2003). Nevertheless, these studies cover distinct but narrow ranges of the Reynolds numbers (respectively $10^5 \leqslant \mathrm{Re} \leqslant 10^6$ and $6 \times 10^2 \leqslant \mathrm{Re} \leqslant 1.2 \times 10^3$), so that a clear trend is hard to recognize.

The flutter derivatives are generally obtained through wind-tunnel tests on oscillatory section models, e.g. in Matsumoto (1996). The computational calculation of these transfer functions is a challenging task for computational fluid dynamics (CFD) and computational wind engineering (CWE). In the latter field of research, the most popular method to achieve this goal was first proposed by Walther and Larsen (1997) and subsequently applied to a number of bridge cross-sections, e.g. in Vairo (2003). The method adopts sinusoidal imposed vibrations of the section in perfect analogy with the experimental tests. The aerodynamic derivatives are obtained from the amplitude and phase relationships between the imposed motion and the fitted time histories of the aeroelastic force components. From a computational point of view, this method is very expensive, as a time-dependent simulation is needed for each nondimensional frequency (the so-called *reduced frequency*) of interest. Moreover, it requires that the extent of the simulated time histories of the aeroelastic force components is large enough to overcome the transient flow solution and to allow their correct fitting. According to the authors, the above-mentioned computational difficulties have not been overcome in a recent study by Le-Maître et al. (2003): the proposed method is based on a spring-mounted airfoil placed in the free-stream, subjected to an initial displacement and then left free to oscillate in order to estimate the apparent damping ratio and apparent natural mechanical frequency of the airfoil. Once more, one simulation is necessary for each reduced frequency of interest. Even though only the transient solution is of interest, the lower the structural frequency, the longer the simulated time and the CPU one. The indicial approach is certainly less expensive from a computational point of view, because of two main reasons. First, a unique simulation is needed to evaluate the transfer function in the whole range of interest of the reduced velocity. Second, only the transient flow has to be simulated, and its extension in time does not depend on the structural natural frequency of the obstacle. Nevertheless, great attention should be paid to make the indicial approach compatible with the computational simulation of the flow. In the authors' opinion, the first attempt made by Brar et al. (1996) to apply the indicial approach by means of CWE experienced some difficulties due to the assumption that the relative angle of attack, associated to a vertical displacement of the section, can be equivalently simulated by a motionless obstacle immersed in a uniform velocity field in space at the initial time. The above-mentioned approach does not respect the physics of the transient flow nor eliminate the numerical errors due to the flow impulsive initial conditions affecting the transient force that arises on the structure. Hence, both the indicial function at its first time steps and its Fourier transform at high frequencies contain a nonphysical contribution. In another work applied to aircraft manoeuvres, Lesieutre et al. (1994) took into account the motion of the wing by directly simulating the imposed obstacle motion. Furthermore, a smoothed-ramp motion of the section during afinite time is proposed in order to overcome the computational problems involved by the step-wise displacement and the infinite velocity of the structure. In a previous work, Fransos and Bruno (2006) extended and adapted the above-mentioned approach to the numerical calculation of the transfer functions expressed in terms of flutter derivatives. The proposed approach has been applied to a thick flat plate immersed in an incoming smooth viscous flow at null mean incidence and at high Reynolds number ($\mathrm{Re} = 10^4$). The efficiency of the approach has been discussed referring to the previous computational results by Walther and Larsen (1997).

The proven low computational cost of the adopted method offers the opportunity, in the present work, of investigating the effects of the Reynolds number on the flutter derivatives of the flat plate for a wide range of Reynolds numbers ($10 \leqslant \mathrm{Re} \leqslant 10^5$). Compressibility effects take place for $\mathrm{Re} < 10$, while the upper bound is close to the theoretical threshold values at which transition to turbulence takes place. The range investigated herein covers both the range of interest for bridge decks and wind turbines ($10^4 \leqslant \mathrm{Re} \leqslant 10^5$) and the one of interest for biomechanics, insect flight and drone planes ($10 \leqslant \mathrm{Re} \leqslant 10^3$).

The key features of the quasi-indicial computational approach employed to identify the flutter derivatives are briefly recalled in Section 2. The Reynolds number effects on the steady and unsteady flow field and on the flutter derivatives are evaluated in Section 3. In particular, the study has been conducted to point out some relationships between the variation of Re, the fluid flow phenomena and the flutter derivatives in order to identify the flow field features that

affect the flutter derivatives to the greatest extent. Hence, an empirical expression of the most important flutter derivatives versus the Reynolds number is proposed.

2. Computational identification of the flutter derivatives

The method adopted herein to compute the 2-D-flutter derivatives follows these steps:

(1) computational simulation of the aerodynamic behaviour of the motionless obstacle with a steady homogeneous incoming flow;
(2) computational simulation of the effects of the motion of the obstacle in the flow:
   (a) the motion (input $i(t)$) is prescribed according to a suitable smoothed-ramp evolution in time;
   (b) the resultant forces (output $o(t)$) are obtained by integration of the surface stresses on the body;
(3) post processing in order to infer flutter derivatives from the simulated time histories of the input $i(t)$ and output $o(t)$ variables.

The main components of the computational model, referring to steps 1 and 2, and the approach employed to recover the flutter derivatives (step 3) are briefly described in the following.

2.1. Computational model

Computational simulation of fluid–structure interaction problems is a challenging task that can be performed through different approaches, depending on the type of interaction and the aim of the simulation. In this paper, the solid structure sub-system is modelled as a 2-D-SDOF rigid body and its dynamics is fully described by the imposed displacement $i(t)$ of its rotational centre. The coupled fluid–structure system is then reduced to a fluid flow in a time-dependent domain, and the motion of the domain boundary is known *a priori*. Time-dependence of the domain introduces a further requirement for grid-based numerical methods, i.e. an efficient way of moving the computational grid.

The following subsections are devoted to describing the mathematical modelling of the fluid flow system, the moving grid strategy and the numerical method employed to solve the obtained model. Nevertheless, it is worth pointing out that the proposed method works for any kind of computational approach and physical model of the flow.

2.1.1. Flow modelling

The incompressible, unsteady, 2-D laminar flow with moving boundaries is modelled in the present study by means of the Navier–Stokes equations. For a moving domain $\Omega_g(t)$, the Arbitrary Lagrangian Eulerian (ALE) approach (Donea, 1996; Nomura and Hughes, 1992) allows a reference frame $\hat{\Omega}_g$ to be introduced, which is mapped for each time t in the fluid domain by $\boldsymbol{\xi} \mapsto \mathbf{x}(t, \boldsymbol{\xi})$, where $\boldsymbol{\xi}$ and $\mathbf{x}$ are the ALE and Eulerian (spatial) coordinates, respectively. The classical nondimensional instantaneous continuity and momentum equations are then modified in their ALE counterpart in terms of the fluid variables relative to the moving frame

$$\begin{cases} \operatorname{div} \mathbf{u} = 0, & \mathbf{x} \in \Omega_g(t),\ t > 0, \\ \left.\dfrac{\partial \mathbf{u}}{\partial t}\right|_{\xi} + (\mathbf{u} - \mathbf{u}_g)\operatorname{grad} \mathbf{u} = -\operatorname{grad} p + \dfrac{1}{\mathrm{Re}}\Delta \mathbf{u}, & \mathbf{x} \in \Omega_g(t),\ t > 0, \end{cases} \tag{1}$$

where $\mathbf{u}$ is the velocity of the fluid, $\partial(\cdot)/\partial t|_{\xi}$ the time derivative on the ALE frame, $\mathbf{u}_g = \partial \mathbf{x}/\partial t|_{\xi}$ the frame velocity, p the pressure. The variables are nondimensionalized by the reference free-stream velocity U, the chord length of the body B and the fluid density ρ, so that the Reynolds number is $\mathrm{Re} = \nu^{-1}$, where ν is the kinematic viscosity. The boundary motion is then treated by imposing

$$\mathbf{u}_g = \frac{\partial \mathbf{x}}{\partial t}, \quad \forall \mathbf{x} \in \partial\Omega_f(t),\ \ t > 0, \tag{2}$$

and solving an auxiliary problem in order to determine $\mathbf{u}_g$ inside the domain. The choice of an appropriate auxiliary problem characterizes the ALE method; the choice adopted in this work is described in Section 2.1.2.

Dirichlet conditions are imposed on the velocity at the inlet and Neumann conditions are imposed on the normal component of the stress tensor $\mathbf{T}$ at the outlet, as depicted in Fig. 1(a).

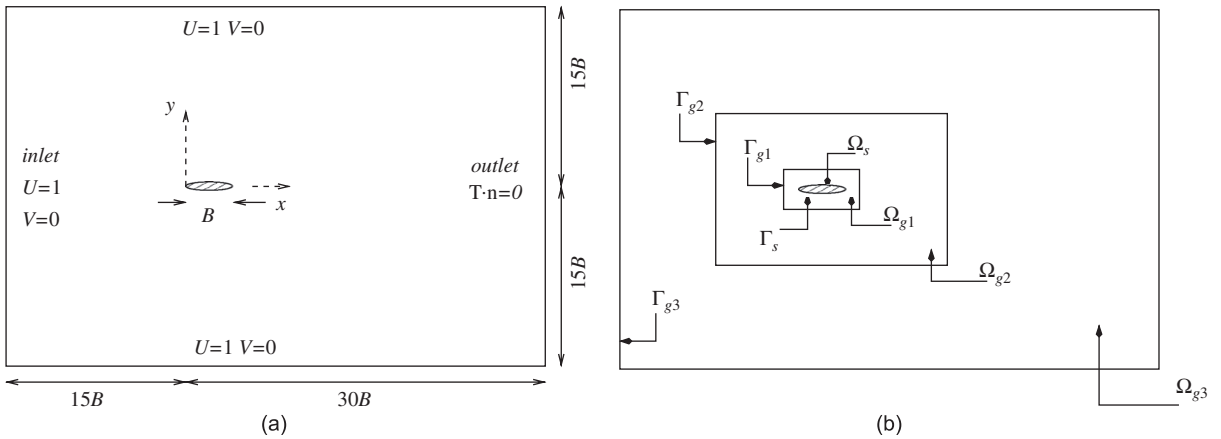

Fig. 1. (a) Computational domain, boundary conditions and (b) partitions for the ALE approach.

The classical Eulerian form of the Navier–Stokes equations can be recovered imposing $\mathbf{u}_g = 0$ in the absence of boundary motion: this choice is adopted to simulate the flow around a motionless obstacle together with no-slip boundary conditions at the wall

$$\mathbf{u} = \mathbf{u}_g = 0, \quad \mathbf{x} \in \Gamma_s, \ \ t > 0, \tag{3}$$

and impulsive initial conditions

$$\mathbf{u}^0 = (U, V), \quad \mathbf{x} \in \Omega_g, \ \ t = 0. \tag{4}$$

The more general ALE approach (Eq. (1)) is used for simulations with a moving obstacle together with the corresponding form of the no-slip boundary condition at the wall

$$\mathbf{u} = \mathbf{u}_g(t) = \mathbf{u}_w(\mathbf{i}(t)), \quad \mathbf{x} \in \Gamma_s, \ \ t > 0, \tag{5}$$

where $\mathbf{u}_w(\mathbf{i}(t))$ is the wall velocity that corresponds to the imposed input obstacle motion $\mathbf{i}(t)$. The velocity field simulated around the motionless obstacle is used as the initial condition for the flow velocity field in moving obstacle problems.

2.1.2. Grid generation strategy

In grid-based methods, two main goals are pursued concerning the mesh in simulating flow problems with moving boundaries. First, the minimization of the computational cost required to adapt the grid to the changes in the domain geometry; second, the maximization of the grid quality at each time step. In order to define it, the ratio $a_i/\Lambda_{\mathbf{x}}$ between the maximum body displacement a_i and the characteristic length of the grid cell $\Lambda_{\mathbf{x}}$ can be assumed as a significant parameter.

On one hand, the application dealt within this paper involves small displacements of the solid boundary, coherently with the assumption of Scanlan's model ($a_i \approx B \times 10^{-2}$). On the other hand, it calls for very fine meshes in order to accurately solve the thin viscous boundary layer at high Re numbers (e.g. $a_i/\Lambda_{\mathbf{x}} \approx 10^2$ at $\mathrm{Re} = 10^4$). The simulation of the unsteady aerodynamics of the moving obstacle also requires a high grid quality in its neighbourhood and in its wake.

Both the decomposition of the computational grid and the deformation of the existing unstructured grid are adopted in the present work in order to handle these features. The artificial field Ω_g of the computational grid is further partitioned by means of a II level decomposition into three sub-fields (Fig. 1(b)) in an analogous manner to Vairo (2003) and Jeong and Kwon (2003).

A hybrid adaptive quad/tri-grid approach is adopted to discretize the resulting complex computational domain. A body-fitted, structured quadrangular grid is generated near the wall in partition Ω_{g1} in order to guarantee the best initial grid quality with orthogonal and unskewed cells. A triangular grid is generated to cover the intermediate domain Ω_{g2} using an advancing front method. Finally, a coarse paved quad grid is used to fill the outer domain Ω_{g3}. The structured quad grid around the solid boundary Γ_s moves with the moving body, while the paved one in Ω_{g3} remains stationary. As the quad grids are not deformed, their quality remains the same along the simulation, which is a particular benefit when solving the viscous boundary layer. In addition, the outer sub-domain Ω_{g3} does not require

re-meshing procedures, thus reducing the computational costs. Meanwhile, the unstructured triangular grid needs to bridge the imposed displacements on Γ_{g1} to the zero-displacements on Γ_{g2}. The deformation of the existing unstructured grid, usually referred to as a "dynamic mesh" approach according to the early work by Batina (1989), is adopted herein for this purpose. In particular, the spring analogy method is adopted to deform the dynamic mesh. The grid in partition Ω_{g2} is viewed as a quasi-static pseudo-structural discrete system. In this analogy, a fictitious lineal spring is attached along each edge connecting two vertices i and j of the fluid mesh, and the stiffness coefficient of this spring is chosen to be inversely proportional to the length l_{ij}^n of the supporting edge at each time step t^n, i.e. $k_{ij}^n \propto 1/l_{ij}^n$, so that if two vertices get closer during mesh motion, the lineal spring attached to the edge connecting the vertices becomes stiffer and therefore prevents them from colliding.

The position of the dynamic mesh is obtained from the solution of the quasi-static problem

$$\begin{cases} \mathbf{q}^n = \bar{\mathbf{q}}^n = y^n + \theta^n \mathbf{r}, & \xi_i \in \Gamma_s, \Omega_{g1}, \Gamma_{g1}, \\ \mathbf{K}^n \mathbf{q}^n = 0, & \xi_i \in \Omega_{g2}, \\ \mathbf{q}^n = 0, & \xi_i \in \Gamma_{g2}, \Omega_{g3}, \Gamma_{g3}, \end{cases} \tag{6}$$

where $\mathbf{q}^n$ is the current displacement vector whose terms are defined by

$$q_i^n = \xi_i^n - \xi_i^0, \tag{7}$$

$\bar{\mathbf{q}}^n$ denotes the prescribed displacement vector of the moving boundary Γ_s of the solid domain Ω_s, $\mathbf{r}$ is the distance between the ith vertex and the centre of rotation O and $\mathbf{K}^n$ is the current stiffness matrix associated to the fictitious lineal springs.

2.1.3. Numerical method

Computations were performed using the FLUENT 6.2 code, based on the Finite Volume Method (Eymard et al., 2000; Ferziger and Peric, 2002).

The physics of the investigated flow seems to be significantly sensitive both to numerical diffusion effects (affecting the smoothing of the velocity defect in the wake of the streamlined obstacle and the small vortical structures induced by its motion) and to numerical dispersion effects (i.e., it appears to cause phase errors between the obstacle displacements and the motion-induced forces acting on it). It is worth observing that the higher the Reynolds number of the flow, the lower the diffusive effects due to kinematic viscosity and the more relevant the numerical diffusion. Thus, the computational simulation of flows characterized by high Reynolds numbers is very sensitive to numerical errors. Advancement in time is accomplished by the first-order implicit Euler scheme. The cell-centre values of the variables are interpolated at face locations using a second-order Central Difference Scheme for the diffusive terms. The interpolation of the convection terms is accomplished by means of the Quadratic Upwind Interpolation for Convective Kinematics (QUICK) on quadrilateral cells in the Ω_{g1} and Ω_{g3} partitions, while the second-order upwind scheme (2UPW) is employed on the triangular cells of the unstructured grid in Ω_{g2}. The local order and the overall leading error made on the flux of a generic variable ϕ by the above-mentioned schemes are summarized in Table 1.

For the sake of simplicity, the overall leading errors are evaluated on a Cartesian equispaced grid for the pure convection equation. The pressure–velocity coupling is achieved by means of the pressure-implicit PISO algorithm, using a predictor–corrector approach for the time discretization of the momentum equation, whilst enforcing the continuity equation.

2.2. Choice of the smoothed-ramp function and motion time

This section briefly mentions the main guidelines followed to select the most suitable smoothed-ramp function $i(t)$ and motion time extension (step 2(a)). The extended *a priori* analysis of the qualitative properties of several smoothed-ramp

Table 1
Adopted numerical schemes

Term	Scheme	Local order	Overall leading error	Main effect
Time	Euler impl.	1st	$\Delta t/2(\mathrm{d}^2\phi/\mathrm{d}t^2)$	Diffusive
Convective	QUICK	3rd	$\Delta x^2/24(\partial^3\phi/\partial x^3)$	Dispersive
	2UPW	2nd	$\Delta x^2/3(\partial^3\phi/\partial x^3)$	Dispersive

functions and the evaluation of the effect of the ramp-time extension on the harmonic content of the function itself can be found in Fransos and Bruno (2006).

In the indicial approach, the Heaviside or step-wise function is traditionally chosen as the input function $i(t)$ because the output function $o(t)$ is the indicial response function itself. In computational applications, a step-wise variation of the imposed displacement cannot be exactly represented because of discretization errors. Moreover, its discrete derivative versus time (velocity) shows large values generally involving nonphysical oscillations of the solution. Hence, a smoothed ramp is preferred. Two main guidelines must be taken into account when choosing the best smoothed ramped input.

First, the input represents a physical, continuous in time, phenomenon, so that a high class of continuity seems a reasonable choice. Lesieutre et al. (1994) proposed a cosine function and a fifth-order polynomial one. In order to guarantee the highest class of continuity, the error function is proposed by the authors:

$$f_{\mathrm{erf}}(t) = \frac{a_i}{2}[1 + \mathrm{erf}(b(t-c))], \quad -\infty \leqslant t \leqslant +\infty, \tag{8}$$

where a_i is the amplitude of the ramp reached after an elapsed "ramp-time" T_r from the start at $t = t_0$. The start time and the ramp-time for the error function are defined as $t_0 \mid i = 0.01a_i$ and $t_0 + T_r \mid i = 0.99a_i$, respectively, because of the asymptotic trend to initial and final values of the function itself. The second guideline refers to the harmonic contents of the input function. Special attention should in fact be paid to assure a significant harmonic content at the upper bound of the range of interest of the reduced frequency $k = \omega B/U$, where $\omega = 2\pi n$ is the angular velocity of the body motion. In the following, a nondimensional ramp-time of $T_r = 0.87$ is retained.

2.3. Identification of the flutter derivatives

In the following, the approach firstly proposed in Fransos and Bruno (2006) to easily recover the 2-D flutter derivatives from the time histories of the body motion and of the acting forces obtained by computational simulation is recalled. Let us consider the expression of the aeroelastic forces arising on an oscillating rigid body immersed in a 2-D wind field given by the model of Scanlan and Tomko, reported in Simiu and Scanlan (1996):

$$L = \frac{1}{2}\rho U^2 B\left[kH_1^*(k)\frac{\dot{y}}{U} + kH_2^*(k)\frac{B\dot{\theta}}{U} + k^2H_3^*(k)\theta + k^2H_4^*(k)\frac{y}{B}\right] \tag{9}$$

and

$$M = \frac{1}{2}\rho U^2 B^2\left[kA_1^*(k)\frac{\dot{y}}{U} + kA_2^*(k)\frac{B\dot{\theta}}{U} + k^2A_3^*(k)\theta + k^2A_4^*(k)\frac{y}{B}\right], \tag{10}$$

where L and M are the lift force and the pitching moment evaluated at the pole $O(0.5B; 0)$, ρ the air density, y and θ the heave and pitch component of the displacement of the pole O, respectively. Herein, the so-called flutter derivatives $H_i^*(k)$ and $A_i^*(k)$ are expressed as functions of the reduced frequency.

The aeroelastic system, because of the basic assumption of the model, can be seen as a linear map (Fig. 2) between the input variables (displacements and velocities) and the output ones (aeroelastic forces).

Hence, Eqs. (9) and (10), obtained for sinusoidal motions, can be generalized to any kind of motion, the proposed smoothed-ramp functions included. Let us consider a general evolution in time $\eta(t)$ of the input variable $\eta = i = y, \theta$ and the corresponding time history of the output variable in nondimensional form $\eta = o = C_L, C_M$ where $C_L = 2L/\rho U^2 B$ and $C_M = 2M/\rho U^2 B^2$. These variables can be expressed as the inverse Fourier transform of their Fourier transform:

$$\eta(t) = \mathscr{F}^{-1}[\mathscr{F}[\eta(t)]] = \int_{-\infty}^{+\infty} a_{\hat{\eta}}(\omega)\mathrm{e}^{\mathrm{j}(\omega t + \varphi_{\hat{\eta}}(\omega))}\mathrm{d}\omega, \tag{11}$$

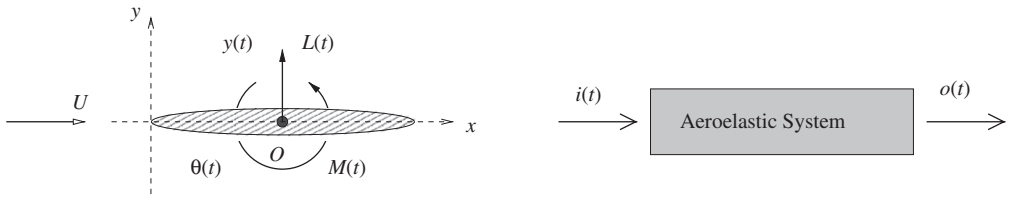

Fig. 2. Aeroelastic forces on a two-dimensional cylinder.

Table 2
Expression of the flutter derivatives

$A_1^*(k)=\dfrac{B}{k^2}\dfrac{a_{\dot{M}}}{a_{\dot{y}}}\sin(\varphi_{\dot{M}}-\varphi_{\dot{y}})$	$H_1^*(k)=\dfrac{B}{k^2}\dfrac{a_{\hat{L}}}{a_{\dot{y}}}\sin(\varphi_{\hat{L}}-\varphi_{\dot{y}})$
$A_2^*(k)=\dfrac{1}{k^2}\dfrac{a_{\dot{M}}}{a_{\hat{\theta}}}\sin(\varphi_{\dot{M}}-\varphi_{\hat{\theta}})$	$H_2^*(k)=\dfrac{1}{k^2}\dfrac{a_{\hat{L}}}{a_{\hat{\theta}}}\sin(\varphi_{\hat{L}}-\varphi_{\hat{\theta}})$
$A_3^*(k)=\dfrac{1}{k^2}\dfrac{a_{\dot{M}}}{a_{\hat{\theta}}}\cos(\varphi_{\dot{M}}-\varphi_{\hat{\theta}})$	$H_3^*(k)=\dfrac{1}{k^2}\dfrac{a_{\hat{L}}}{a_{\hat{\theta}}}\cos(\varphi_{\hat{L}}-\varphi_{\hat{\theta}})$
$A_4^*(k)=\dfrac{B}{k^2}\dfrac{a_{\dot{M}}}{a_{\dot{y}}}\cos(\varphi_{\dot{M}}-\varphi_{\dot{y}})$	$H_4^*(k)=\dfrac{B}{k^2}\dfrac{a_{\hat{L}}}{a_{\dot{y}}}\cos(\varphi_{\hat{L}}-\varphi_{\dot{y}})$

where $a_{\hat{\eta}}(\omega)$ and $\varphi_{\hat{\eta}}(\omega)$ are the modulus and the phase angle of the Fourier transform of $\eta(t)$, respectively. If a linear operator is assumed to map the input and output, for each reduced frequency, the argument of the integral in Eq. (11) can be expressed by means of Eqs. (9) and (10). For instance, let us consider $\theta(t)$ as the input and $C_L(t)$ as the output. Using the Scanlan and Tomko formulation, one obtains:

$$a_{\hat{L}}e^{j(\omega t+\varphi_{\hat{L}})}=\left[kH_2^*\frac{B}{U}\frac{d}{dt}(a_{\hat{\theta}}e^{j(\omega t+\varphi_{\hat{\theta}})})+k^2H_3^*a_{\hat{\theta}}e^{j(\omega t+\varphi_{\hat{\theta}})}\right]=k^2a_{\hat{\theta}}[jH_2^*+H_3^*]e^{j(\omega t+\varphi_{\hat{\theta}})}. \tag{12}$$

It follows that

$$H_3^*+jH_2^*=\frac{1}{k^2}\frac{a_{\hat{L}}}{a_{\hat{\theta}}}e^{j(\varphi_{\hat{L}}-\varphi_{\hat{\theta}})}=\frac{1}{k^2}\frac{a_{\hat{L}}}{a_{\hat{\theta}}}(\cos(\varphi_{\hat{L}}-\varphi_{\hat{\theta}})+j\sin(\varphi_{\hat{L}}-\varphi_{\hat{\theta}})), \tag{13}$$

and equating the real and imaginary components:

$$H_2^*(k)=\frac{1}{k^2}\frac{a_{\hat{L}}}{a_{\hat{\theta}}}\sin(\varphi_{\hat{L}}-\varphi_{\hat{\theta}}),\quad H_3^*(k)=\frac{1}{k^2}\frac{a_{\hat{L}}}{a_{\hat{\theta}}}\cos(\varphi_{\hat{L}}-\varphi_{\hat{\theta}}). \tag{14,15}$$

In an analogous manner the expressions of the remaining six flutter derivatives are easily obtained and are listed in Table 2. Eqs. (14) and (15) show that it is possible to determine the transfer function in the frequency domain for any input by evaluating the ratio between the Fourier transforms of output $o(t)$ and input $i(t)$, provided the inverse of the latter is not singular. Furthermore, the modulus of the Fourier transform of input $a_{\hat{i}}(\omega)$ must be large enough with respect to the one of the output $a_{\hat{o}}(\omega)$ at every frequency of interest, in order to guarantee the accurate numerical evaluation of the flutter derivatives. Finally, it is worth noting that the method can also be applied to the classical Heaviside input function, where $a_{\hat{i}}=1$ and $\varphi_{\hat{i}}=0$.

3. Reynolds number effects

The proposed approach is applied to the parallel incoming laminar flow along a finite-length smooth flat plate. A finite thickness $D=B/400$ and rounded leading and trailing edges are adopted to obtain a streamlined section.

The Reynolds number effects on the steady flow past the motionless obstacle and on the unsteady flow around the moving plate are systematically investigated in the following. The efficiency of the proposed computational approach, proven in Fransos and Bruno (2006), allows the computational solution of the Navier–Stokes equations in a wide range of Re values ($10\leqslant Re\leqslant 10^5$). The flow is incompressible and laminar in this range, while compressibility effects take place for $Re<10$, as shown by Sun and Boyd (2004), and the transition from the laminar boundary layer to the turbulent one occurs at $Re_{x,crit}=\approx 3\times 10^6$, according to the boundary layer theory (Schlichting, 1979).

Apart from the previously illustrated grid-generation strategy, the density of the control volumes (cv) is mainly dictated by two problem-dependent aspects. First, the highest grid density is set in the obstacle neighbourhood by imposing a cell thickness close to the wall $y_w=5\times 10^{-6}B$ in order to accurately resolve the laminar wall boundary layer. Even though the accurate simulation of the flow in the neighbourhood of the plate plays a dominant role in steady aerodynamics, an analogous precision is required to predict the velocity distribution in the wake in view of the study of the aeroelastic behaviour. The indicial response in fact quantifies the effect of the impulsive-motion-induced flow field perturbations and of their following convection far from the obstacle in its wake on the aeroelastic forces. Hence, the accurate computational simulation of the transport mechanisms (convection and diffusion) along the wake plays a relevant role in predicting flutter derivatives at high reduced velocities $U_r=1/k=U/nB$. The extended analysis

of the effects of the grid density in the wake region on the computational results can be found in Fransos and Bruno (2006). In the following, the adopted computational grid in the region downwind to the trailing edge is characterized by a nondimensional cv surface $A_{cv}/B^2 = 10^{-4}$. The region cross-wind dimension is equal to $0.2B$ while its alongwind extension is equal to $8B$. The overall grid cv number is equal to 10.5×10^4.

3.1. Steady-state flow past a fixed plate

The aerodynamic behaviour of a fixed plate in a steady viscous flow is first simulated to provide suitable initial conditions for the simulation with a moving obstacle and to compare the computational results with the available analytical solutions. In particular, the results obtained are compared to Blasius and Goldstein closed-form solutions, as well as to some experimental data available in literature. It is worth recalling that Blasius assumptions fully hold for $\mathrm{Re} \geqslant 10^3$: hence, only data for this range are reported.

Fig. 3 shows the main characteristics of the boundary layer around the plate. Its shape can be observed in Fig. 3(a), where the $0.99U$ contour of the velocity is plotted.

The Reynolds number affects not only the boundary layer thickness along the side of the plate, defined as the nondimensional distance from the wall y/B at which $u_x = 0.99U$, but also the width of the front region, which is far from being negligible at low Re even for a thin flat plate. It is worth pointing out that the shape of the front region also depends on the leading edge geometry of the plate. The growth of the boundary layer thickness along the upper side of the plate is shown in Fig. 3(b): a general good agreement results from the comparison with the closed-form Blasius solution. Similar conclusions can be drawn for the velocity profile along the $x/B = 0.5$ line, which is plotted in Fig. 3(c). In both cases, the profiles at $\mathrm{Re} < 10^3$ vary with the same trend, but cannot be compared with any approximate closed-form solution. Fig. 4(a) shows the horizontal velocity along the $y/B = 0$ line, while the horizontal component of the velocity along the $x/B = 1.5$ line is plotted in Fig. 4(b). In both cases, the results obtained are compared to the experimental and theoretical values reported by Goldstein. The discrepancy between the present results and the reference values in the maximum horizontal velocity defect in the near wake is probably related to the finite thickness of the plate. Fig. 5(a) shows the skin friction coefficient distribution along the side of the plate at different Reynolds numbers.

The friction coefficient regularly varies in agreement with Blasius solution in the range of validity of the latter. The distribution along the plate does not significantly vary for lower values of Re, but the pointwise value of the friction coefficient (e.g. at $x/B = 0.5$ in Fig. 5(b)) increases more quickly than Blasius solution as the Re number decreases. In the $10 \leqslant \mathrm{Re} \leqslant 100$ range, the trend of the computational results is best fitted to $C_f \propto \mathrm{Re}^{-2/3}$. Fig. 6(a) shows the pressure coefficient distribution along the side of the plate at different Reynolds numbers. The pressure distribution along the side surfaces tends to the one around the thin plate ($C_p = 0$) at high Re numbers. On the contrary, the suction on the lateral surfaces significantly increases between $\mathrm{Re} = 400$ and $\mathrm{Re} = 100$, highlighting two distinct flow regimes around these watershed values. Moreover, the pressure coefficient at the stagnation point $C_{p_{sp}}$ (see Fig. 6(b)) is not equal to the unit at each Re as the Bernoulli equation states for a perfect fluid. The obtained data show that the lower the Re, the higher the C_p at $x/B = 0$ and that the latter asymptotically tends to the unit when the former increases.

When Re decreases, the diffusive term due to viscosity in the Navier–Stokes equations cannot be neglected with respect to the convective one. As previously pointed out in Khris (1998), diffusion can be considered as an energy loss that adds to the kinetic energy loss that arises near the stagnation point. The momentum conservation forces the gradient pressure $\mathrm{d}p/\mathrm{d}x$ to react to these energy losses, and this reaction causes the high pressure at the stagnation point. In other words, from an energetic point of view, the Bernoulli equations can be rewritten in a more general form as $C_{p_{sp}} = 1 + \Delta H_p$, where $\Delta H_p > 0$ is the pressure energy surplus. The fitting of $C_{p_{sp}}$ versus Re in Fig. 6(b) would suggest expressing the pressure energy surplus as $\Delta H_p = 76.67/\mathrm{Re}^{2/3}$, revealing the same dependence versus Re that has previously been pointed out for the friction coefficient along the plate.

The resultant aerodynamic force is reduced to the drag component due to flow symmetry. The overall drag coefficient C_D is split into its C_{Dp} and C_{Df} components, due to the pressure and the shear stresses, respectively. Their evolution versus Re is shown in Fig. 7(a). It clearly appears that the friction component is predominant at each Re number, as can be expected in the case of streamlined bodies.

Fig. 7(b) compares the obtained values of the overall drag coefficient C_D, varying the Reynolds numbers, with the experimental results available in literature (Sun and Boyd, 2004; Dickinson and Gotz, 1993; Sunada et al., 1997; Schaaf and Sherman, 1954) and with the Blasius solution. The present results are in excellent agreement with all the reference values. It is worth noting that, as for the friction coefficient, the drag coefficient shows a change in its dependence on Re between $\mathrm{Re} = 100$ and $\mathrm{Re} = 400$. While Blasius pointed out this dependence to be $C_D \propto \mathrm{Re}^{-1/2}$ for $\mathrm{Re} \geqslant 1000$, the experimental and computational data for $\mathrm{Re} \leqslant 100$ are best fitted to $C_D \propto \mathrm{Re}^{-2/3}$.

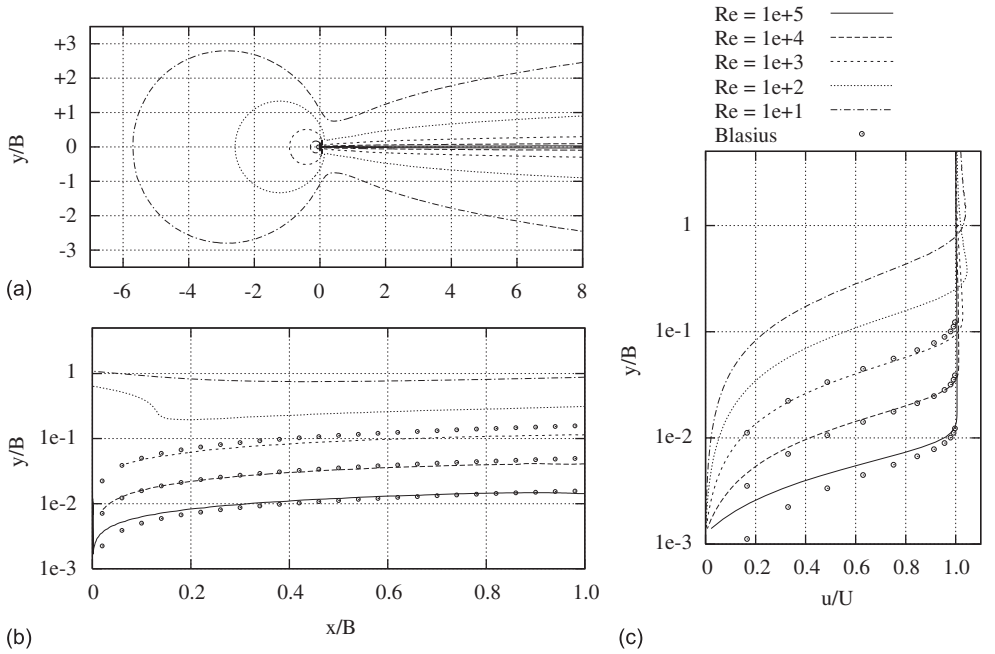

Fig. 3. Boundary layer thickness around the plate and velocity profile at $x/B = 0.5$ varying Re.

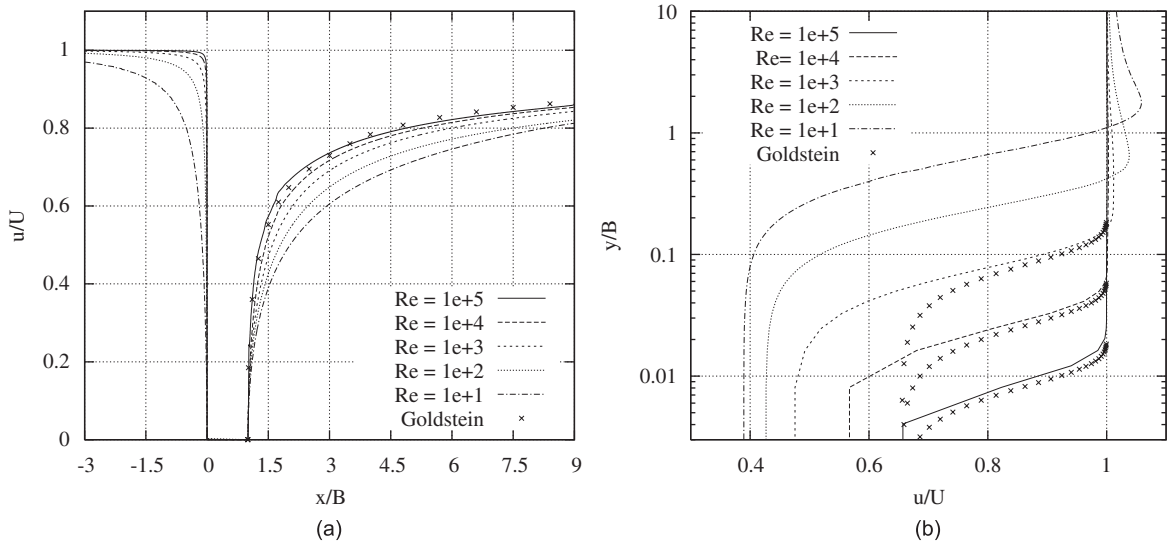

Fig. 4. Horizontal component of the velocity in the wake at different Re numbers.

3.2. Unsteady-state flow past a moving plate

In this section, the study deals with the flat plate aeroelastic behaviour at different Reynolds numbers. A smoothed-ramp motion is imposed on the obstacle according to the approach previously described in order to recover its aeroelastic coefficients. The motion is applied to a single degree of freedom, heaving or pitching, at a time. The amplitude of the prescribed smoothed ramp is chosen in order to fulfill the assumption of small displacements and velocities of the wall, so to avoid the boundary layer separation and guarantee the linearity of the aeroelastic system. Hence $a_\theta = +1^\circ$ (counterclockwise) is adopted for the pitch rotation around the torsional axis at the mid-chord of the

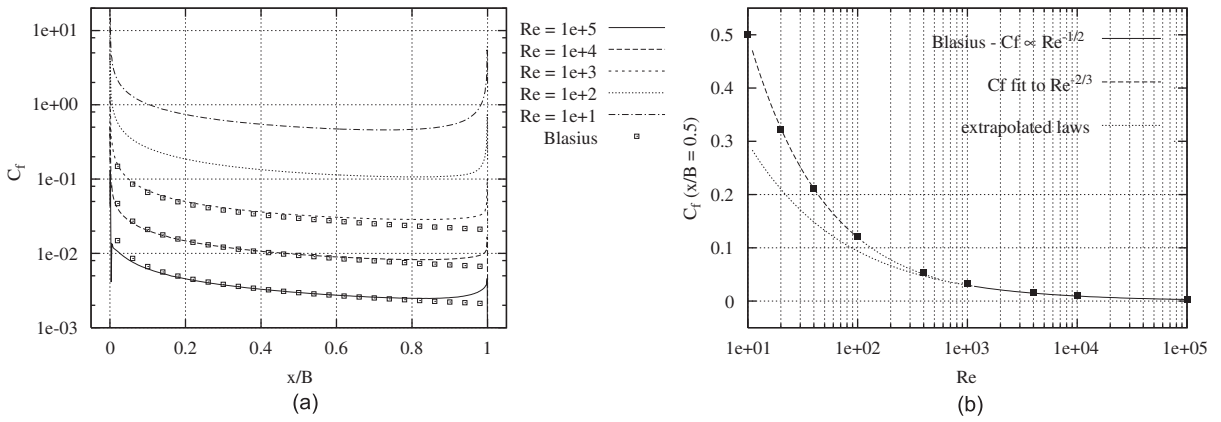

Fig. 5. C_f distribution along the plate and at $x/B = 0.5$, varying Re.

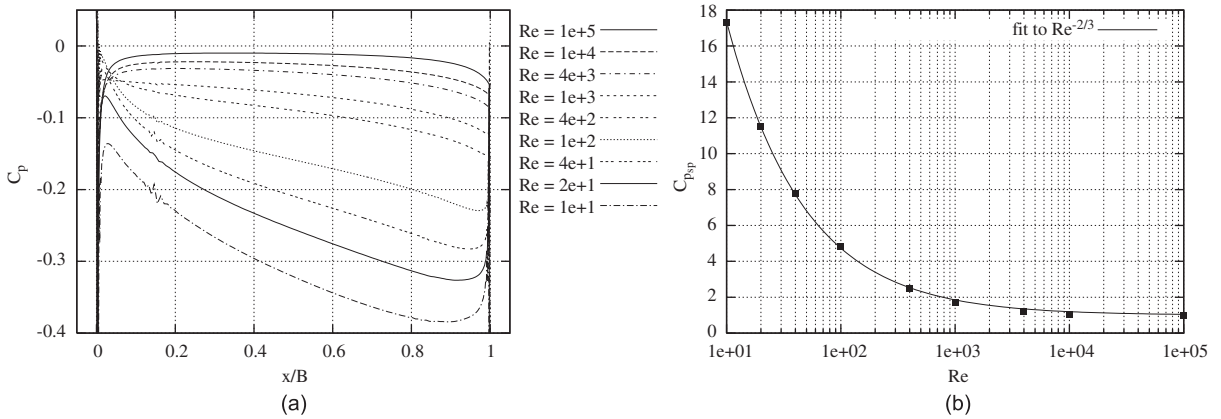

Fig. 6. C_p distribution along the plate and at $x/B = 0$, varying Re.

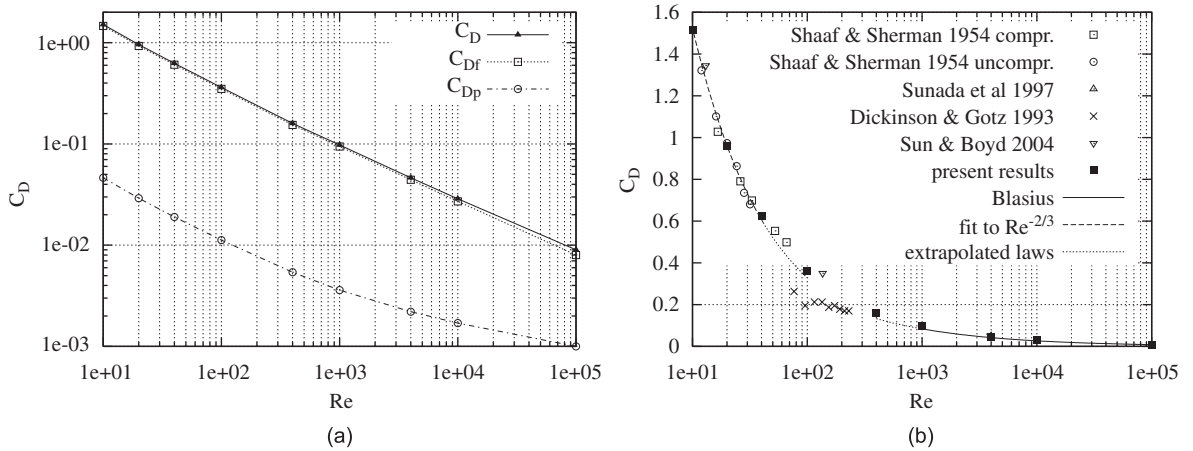

Fig. 7. Drag coefficient varying Re: components and total value.

plate. The heaving amplitude is then fixed to obtain the same maximum wall velocity at the tips of the plate, i.e. $a_y = +8.7 \times 10^{-3} B$. The computational simulation of the unsteady flow is performed assuming a time step $\Delta s = 10^{-3}$, where $s = tU/B$ is the nondimensional time unit. High discretization density in time is required to provide an accurate description of the ramped motion along $T_r = 0.87s$ and in order to reduce the diffusive effect of the truncation error caused by the first-order implicit Euler scheme. The computational simulation is carried out till the asymptotic values of the aerodynamic forces are reached (nondimensional time unit $s = tB/U \approx 50$).

The lift (first row) and moment (second row) coefficients that arise on the obstacle due to heaving (first column) or pitching (second column) motion, are plotted in Fig. 8 versus the shifted time $\Delta s = s - T_r/2$, where T_r is the time required to accomplish the motion. The forces show common behaviour of their evolution in time. A local maximum occurs during the motion of the plate: in particular, the Reynolds number effects on these forces (in the following referred to as *in-motion* forces) dramatically affect the diagonal terms (lift coefficient due to heaving motion and moment coefficient due to pitching motion). Once the obstacle is motionless, the forces (in the following referred to as *post-motion* forces) monotonically tend to the asymptotic steady value, even though the latter is more clearly observable in the extra diagonal coefficients (lift coefficient due to pitching motion and moment coefficient due to heaving motion). In the following, both trends are discussed in order to first interpret them from a phenomenological point of view and then to find dependencies of some significant quantities on the Reynolds number for each of them. As regard the in-motion forces, let us focus for instance on the lift coefficient during the heaving motion. As for the moment coefficient due to pitching motion, it shows a different evolution in time at very low ($\mathrm{Re} \leqslant 100$) and high ($\mathrm{Re} \geqslant 400$) Reynolds numbers, analogously with the aerodynamic behaviour in a steady flow. For $\mathrm{Re} \leqslant 100$, the obstacle is subject to an increasing upward lift during its upward motion (Fig. 9(a)).

In order to better understand this phenomenon, let us look at the pressure coefficient and at the vertical component of the friction coefficient along the upper surface for $\mathrm{Re} = 10$ at five sampled time steps (Fig. 9(b) and (c)). The pressure increases at the upper surface with the velocity of the motion, as can be expected, reaching its maximum at $s = T_r/2$. The lower surface is subjected to a suction that is equal in magnitude and with a null time delay. The lift term resulting from the pressure is therefore negative in the global reference system (downwards). The positive overall lift can only be given by the contribution of the vertical component of the viscous forces. In fact, its magnitude reaches higher instantaneous values than the pressure, which are equal in sign and magnitude at both the upper and lower surfaces. In order to explain how these forces occur, let us look at the relative velocity U_{rel} between the plate surface and the fluid, as sketched in Fig. 10.

Even though the plate keeps an absolute zero angle of attack α during the whole vertical motion, the relative velocity shows a vertical component that is equal to the motion velocity, while the horizontal component U_t remains the same as that of motionless plate. Hence, the shear stress τ at the wall even has a vertical component along the flat surfaces of the plate. Bearing in mind that shear stresses are proportional to the kinematic viscosity $\nu = \mathrm{Re}^{-1}$, the lower Re, the higher the vertical component τ_y. Hence, the vertical component of the shear stress τ_y gives positive resultant forces in the global reference system (upwards) both on the upper and lower surfaces, that sums and prevails on the pressure contribution in the lift coefficient.

The evolution in time of the lift differs for high Reynolds numbers ($\mathrm{Re} \geqslant 400$ in our study, Fig. 11), showing both local minimum and maximum values.

As expected, the friction contribution to the lift becomes negligible, and the whole behaviour of the lift is therefore driven by the instantaneous pressure distribution on the plate surfaces, which is plotted for the sampled time steps at $\mathrm{Re} = 10^5$ in Fig. 11. During the first part of the motion, the plate is accelerated upwards and the inertial effects cause the pressure to assume very high positive values at the upper surface and weakly negative values at the lower surface. Hence, the resulting lift force is negative in the global coordinates. For $s > T_r/4$, the acceleration decreases and, for the same reason as before, the pressure changes sign at the lower surface and becomes weaker at the upper surface. Hence, the lift coefficient changes sign becoming positive, before tending to zero when the motion ends.

In order to investigate the dependence of the in-motion forces from Re, let us consider the maximum value of the in-motion aerodynamic coefficients $C_{i,j}$ (circles in Figs. 9 and 11) and their time delay $P_{i,j}$ from $\Delta s = 0$, at which the maximum velocity occurs (Fig. 12).

The maximum values are shown to be proportional to $1/\sqrt{\mathrm{Re}}$ (Fig. 12(a)), highlighting a linear dependence on the kinematic viscosity. On the contrary, no unique fitting of the time delay is possible in the whole explored range of Re (Fig. 12(b)). Coherently with what has been discussed above, it is possible to distinguish two different ranges in which the dependence changes: for $10 \leqslant \mathrm{Re} \leqslant 10^2$ the lift time delay is proportional to $\mathrm{Re}^{1/3}$ and the moment time delay is proportional to $\mathrm{Re}^{2/3}$, while in $4 \times 10^2 \leqslant \mathrm{Re} \leqslant 10^5$ both are proportional to $1/\sqrt{\mathrm{Re}}$. It is worth noting that the forces are in phase with the velocity at the lowest Re (showing the prevalence of the viscous term), while the lift force tends to be in phase with acceleration (time delay $P_{L,y} = T_r/4$) at the highest Re, showing the prevalence of the inertial effects. The dynamics of the vortex shed in the wake from the trailing edge of the moving plate is analysed in the following, in order

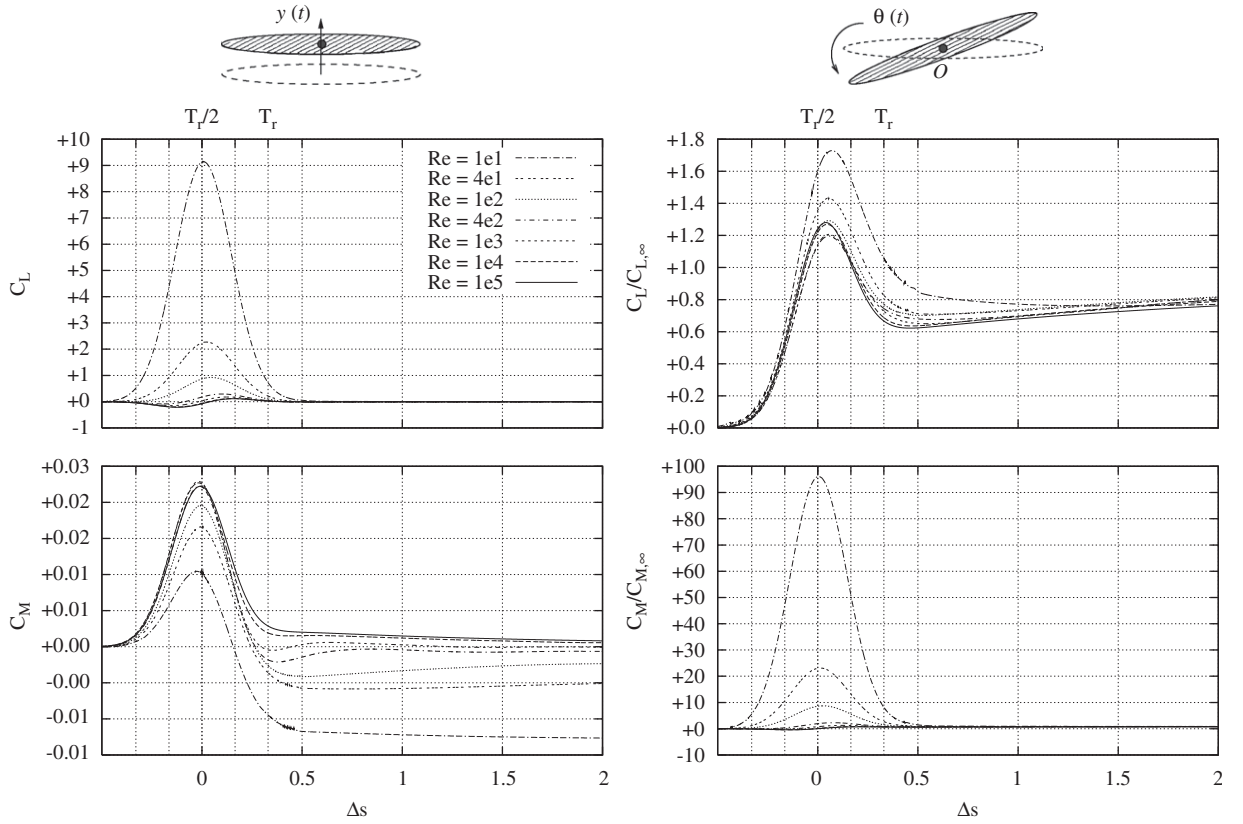

Fig. 8. Unsteady aerodynamic coefficients due to heaving or pitching smoothed-ramp motion.

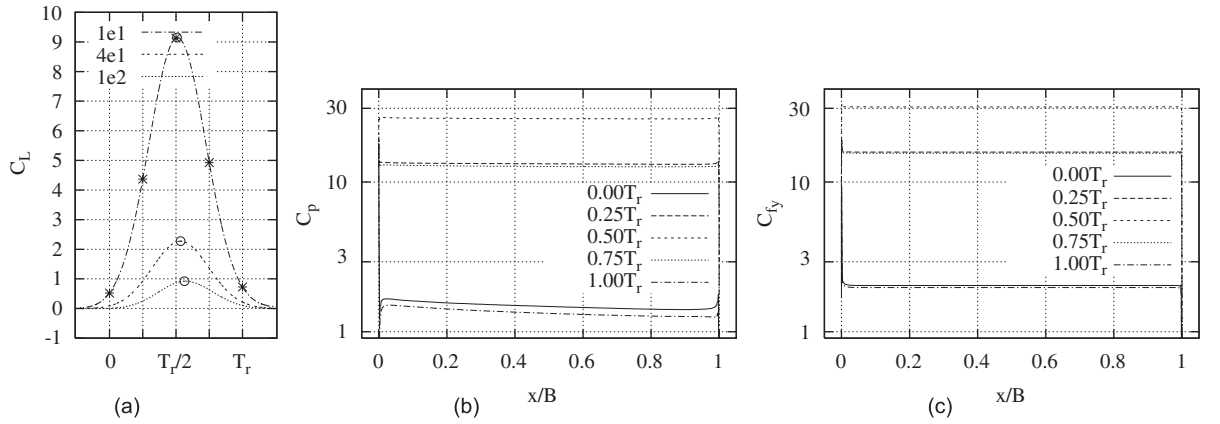

Fig. 9. Re = 10: pressure coefficient and vertical component of the wall shear stress coefficient at the upper surface during the upwards heaving motion.

to study the influence of the Reynolds number on the post-motion forces, From a qualitative point of view, the evolution of the aerodynamic forces acting on the plate after it stops moving are expected to be due to the perturbation induced in the flow field by the vortex itself. From this point of view, both the velocity at which the vortex is convected and its diffusion play relevant roles on the rate of change of the aerodynamic forces. The instantaneous wake structure at the time $s = T_r/2 + \Delta s$, with $\Delta s = 3.5$, is visualized in Fig. 13(a) by means of the vorticity contours, while the position of the vortex core at the same time is estimated by the abscissa corresponding to $u_y = 0$ on the line $y/B = 0$ for different Re (Fig. 13(b), circles).

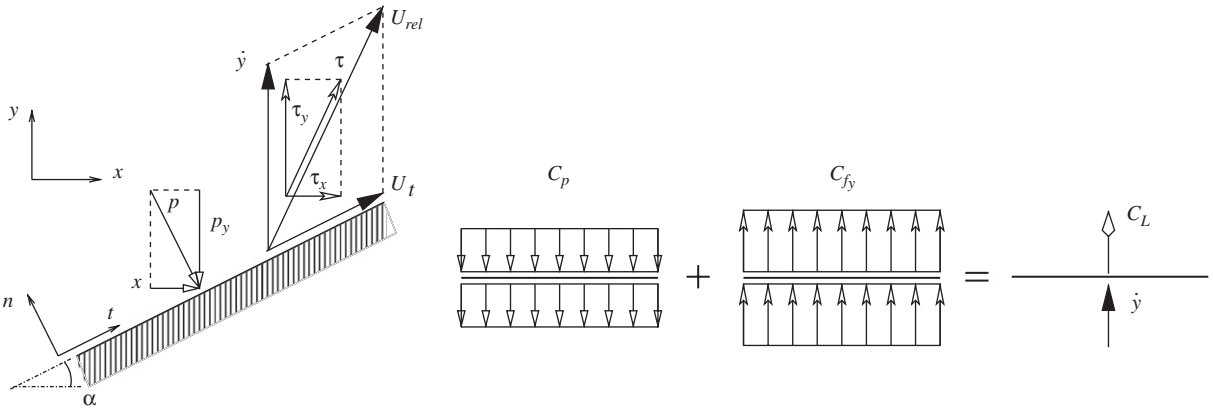

Fig. 10. Scheme of the motion-induced force components at low Reynolds number ($Re \leqslant 100$).

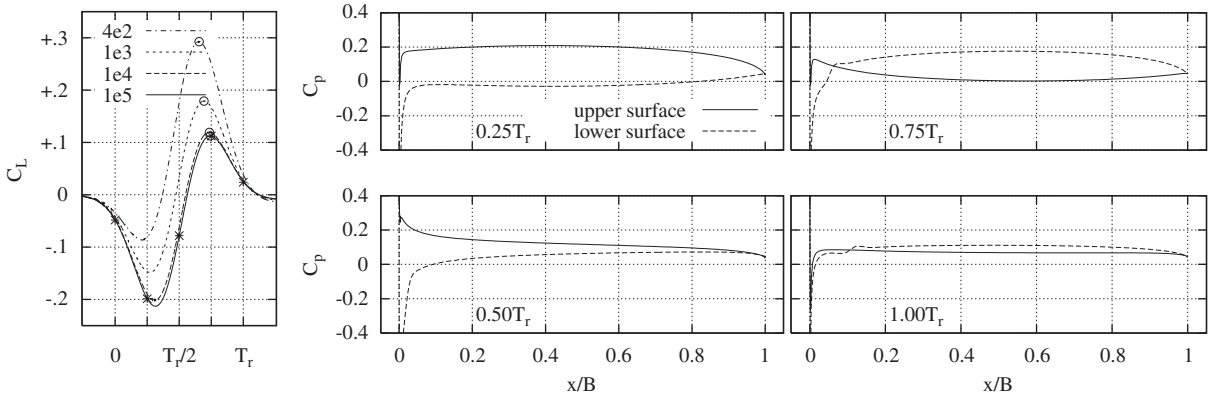

Fig. 11. $Re = 10^5$: pressure coefficient at the upper and lower walls during the motion.

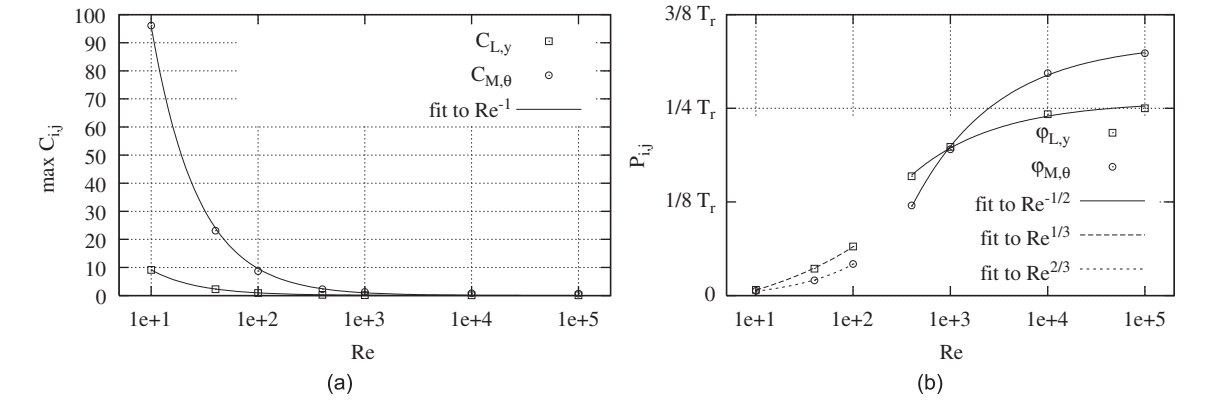

Fig. 12. In-motion forces dependency on Re number.

It is worth noting that the wake becomes much thinner than the perturbation at high Re: this causes the perturbation itself to be greatly affected by the undisturbed flow that impacts on it and consequently to generate other velocity fluctuations characterized by smaller scales nearby.

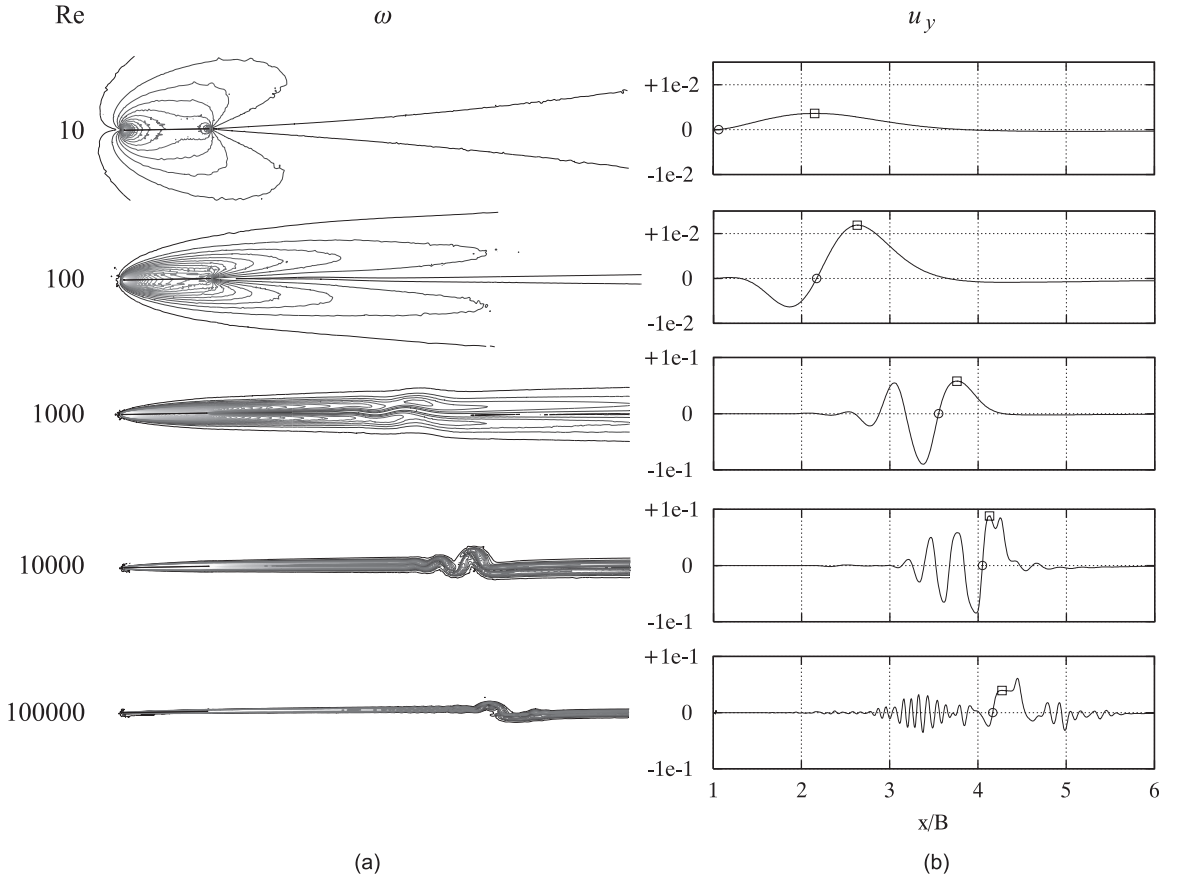

Fig. 13. Vorticity magnitude field and y-velocity along line $y/B = 0$ in the wake for different Re at $s = T_r/2 + 3.5$.

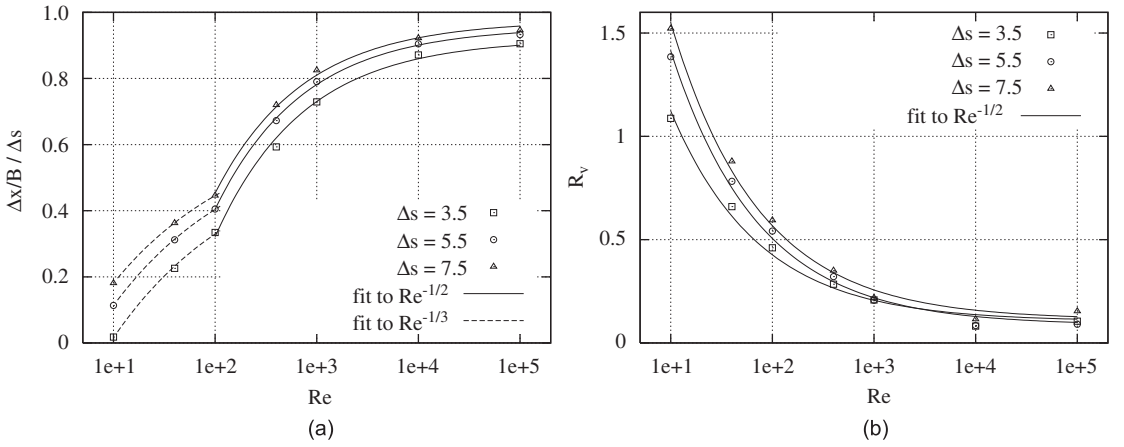

Fig. 14. Convection and diffusion terms dependency on Re number.

The distance $\Delta x/B$ traveled by the vortex from when the plate stops moving ($s = T_r/2$) is obtained as the difference between the abscissa of the zero value of u_y (highlighted by circles in Fig. 13(b)) and the abscissa of the trailing edge. Hence, an estimate of the averaged convective velocity is obtained as $\Delta x/(B\Delta s)$ for various Δs and Re (Fig. 14(a)).

Analogously to the time delay of the in-motion forces, no unique fitting of the convection velocity versus Re is possible: a dependence on $1/\sqrt[3]{\mathrm{Re}}$ is observed at low Reynolds numbers, while this dependence is on $1/\sqrt{\mathrm{Re}}$ at the high

ones. It is worth noting that the convective velocity of the vortex asymptotically tends to the undisturbed flow field velocity (thin wake) for increasing Re. The higher the Re, the thinner the wake and the higher the convection velocity at which the motion-induced vortex is transported. Bearing in mind that the latter is the flow structure that mainly affects the post-motion force evolution in time, its components C_L and C_M are expected to tend faster to their steady values.

The radius R_v of the vortex initially shed from the plate is estimated for various Δs and Re as the distance between the u_y zero value (e.g. in Fig. 13(b), circles) and its closer downwind local maximum (e.g. in Fig. 13(b), squares). A dependence on $1/\sqrt{\mathrm{Re}}$ can be observed for this quantity in the whole range of Re (Fig. 14(b)).

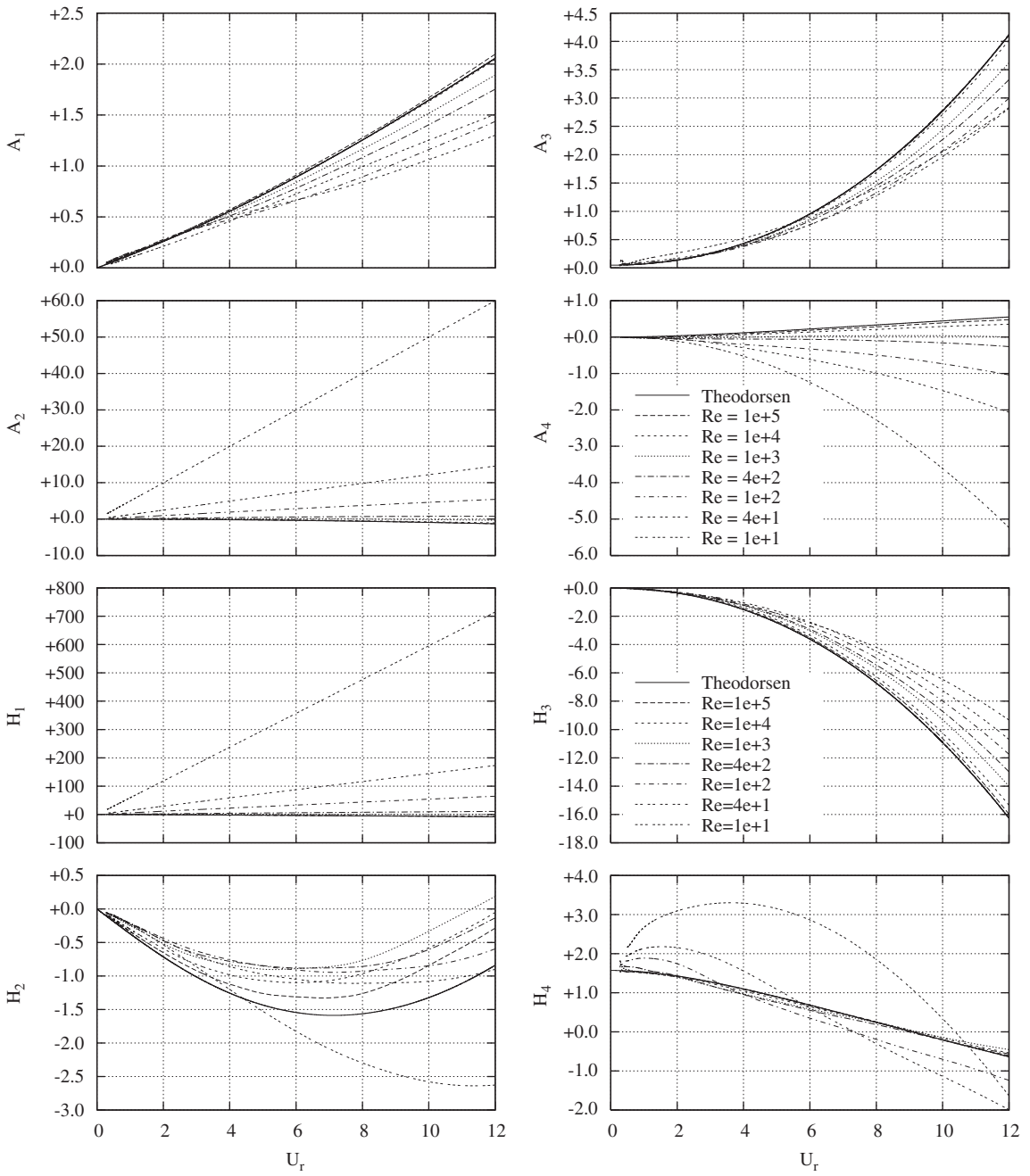

Fig. 15. Flutter derivatives at different Reynolds numbers.

3.3. Flutter derivatives

The flutter derivatives, computed for each Re using the presented method are plotted in Fig. 15 and compared with the closed-form solution obtained with the Theodorsen function. All the derivatives show a relevant dependence on the Reynolds number and tend to the Theodorsen solution (inviscid flow) for increasing Re. The results obtained at $\mathrm{Re} = 10^5$ show an excellent agreement with the analytical results, except for the H_2 and A_4 ones. It is worth noting that the absolute value of H_1 and A_2, that is the flutter derivatives of main interest in torsional and coupled flutter, varies by two orders of magnitude across the range of Re at each U_r.

In order to better understand the differences between the flutter derivatives that are analytically available for inviscid flows and the ones numerically obtained for low Re flows, the percentage scatter averaged on U_r is plotted for each derivative in Fig. 16. Significant scatter, ranging from 5% to 100%, can be observed for all the derivatives in the bridge deck and wind turbine range of interest ($10^4 \leqslant \mathrm{Re} \leqslant 10^5$). The A_2 and H_1 derivatives exhibit even greater scatters (up to 10 000%) for the biomechanics and drone plane Re numbers of interest ($10 \leqslant \mathrm{Re} \leqslant 10^3$).

Bearing in mind the Reynolds number dependencies previously highlighted for some of the main flow quantities (Figs. 12 and 14), the flutter derivatives are fitted versus Re using the following functions:

$$\begin{aligned} F_i(\mathrm{Re}, U_r) &= a\mathrm{Re}^{-1} + b\mathrm{Re}^{-1/3} + c\mathrm{Re}^{p}, \quad 10 \leqslant \mathrm{Re} \leqslant 10^2, \\ F_i(\mathrm{Re}, U_r) &= F_i^*(U_r) + a\mathrm{Re}^{-1} + b\mathrm{Re}^{-1/2}, \quad 4 \times 10^2 \leqslant \mathrm{Re} \leqslant 10^5, \end{aligned} \tag{16}$$

where $F_i = [A, H]$ are the Reynolds-dependent flutter derivatives with $i = [1, 4]$, F_i^* the flutter derivatives obtained from the Theodorsen function, $p = \frac{1}{3}$ for $i = y$ and $p = \frac{2}{3}$ for $i = \theta$. The obtained fittings versus Re are shown in Fig. 17. On the one hand, the excellent fits (except for H_2 and H_4) confirm that the most significant features of the interaction phenomena and their dependence on Re were recognized with adequate accuracy in the previous section. On the other hand, generally speaking, the flutter derivatives exhibit a different dependence on Re in the same two ranges pointed out in the previous sections. Roughly speaking, A_2, H_1, H_3 and A_4 show monotonic behaviour for increasing Re in both ranges, while the remaining derivatives do not. In particular, the regular trends of A_2, H_1 and A_4 versus Re would lead us to think that a unique variation law versus Re can be found. In particular, these derivatives change sign at low Reynolds numbers ($\mathrm{Re} \leqslant 10^3$), revealing possible unstable aeroelastic behaviour of the profile. Bearing in mind the prevailing role played by H_1 and A_2 in flutter and their high sensitivity to Re, a further fitting was proposed according to the simplified function:

$$F_i = F_i^* + \frac{a}{\mathrm{Re}} + \frac{b}{\sqrt{\mathrm{Re}}}, \tag{17}$$

which retains the dependencies found for the maximum value of the in-motion forces and for the vortex diffusion in the wake, both spanning along the whole range of Re. The fitting is plotted in Fig. 18(a). The fitting coefficients are plotted versus U_r in Fig. 18(b) in order to point out the linear and quadratic dependencies, respectively. Hence, the approximated expression of these derivatives as functions of Re and U_r are

$$A_2 \approx A_2^* + 49\frac{U_r}{\mathrm{Re}} + 0.09\frac{U_r^2}{\sqrt{\mathrm{Re}}}, \quad H_1 \approx H_1^* + 594\frac{U_r}{\mathrm{Re}} + 0.7\frac{U_r^2}{\sqrt{\mathrm{Re}}}. \tag{18}$$

The contribution of the in-motion force amplitude clearly prevails on the vortex diffusion in the wake.

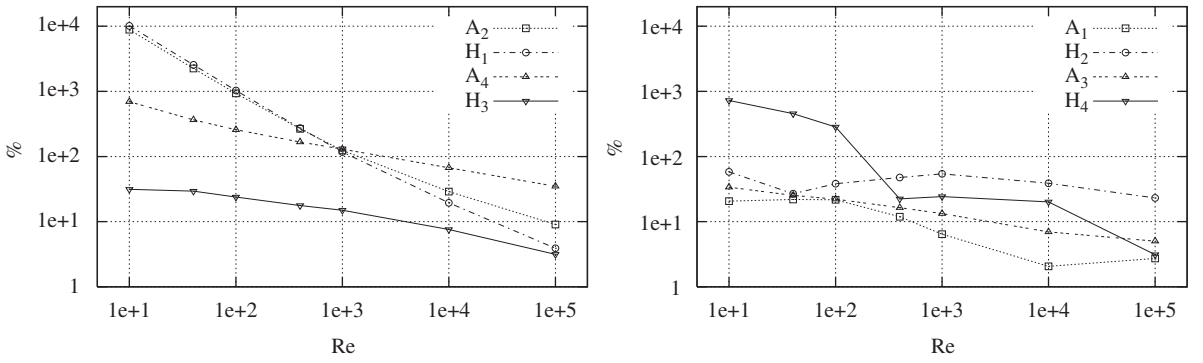

Fig. 16. Scatter from Theodorsen solution (potential flow).

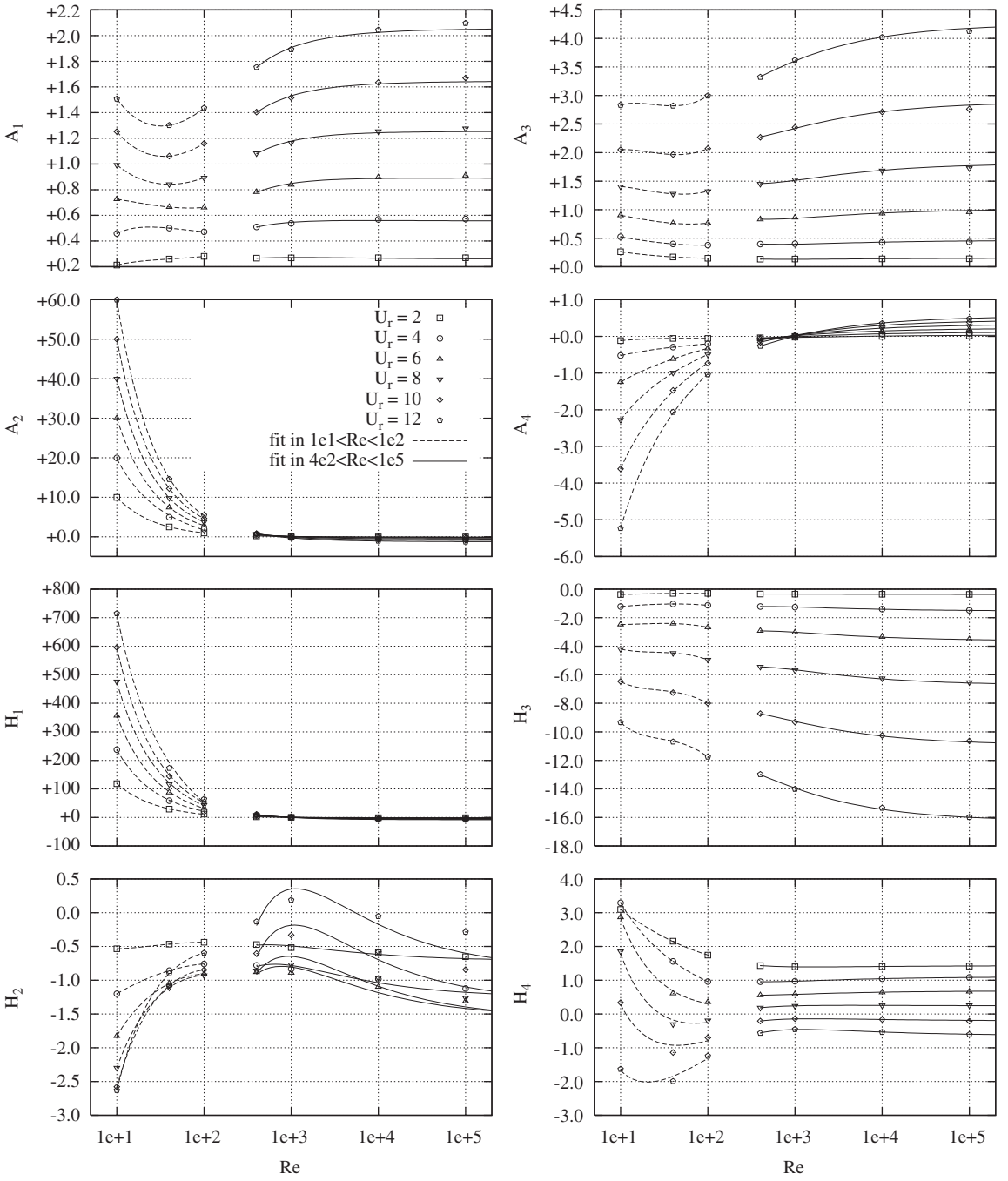

Fig. 17. Flutter derivatives versus Re at given U_r values: two-Re-range fitting.

4. Conclusions

The possibility of estimating flutter derivatives for a streamlined body through computational simulation of the flow around a moving obstacle is analysed in this paper. The classical indicial approach is modified in order to guarantee its compatibility with the computational tool.

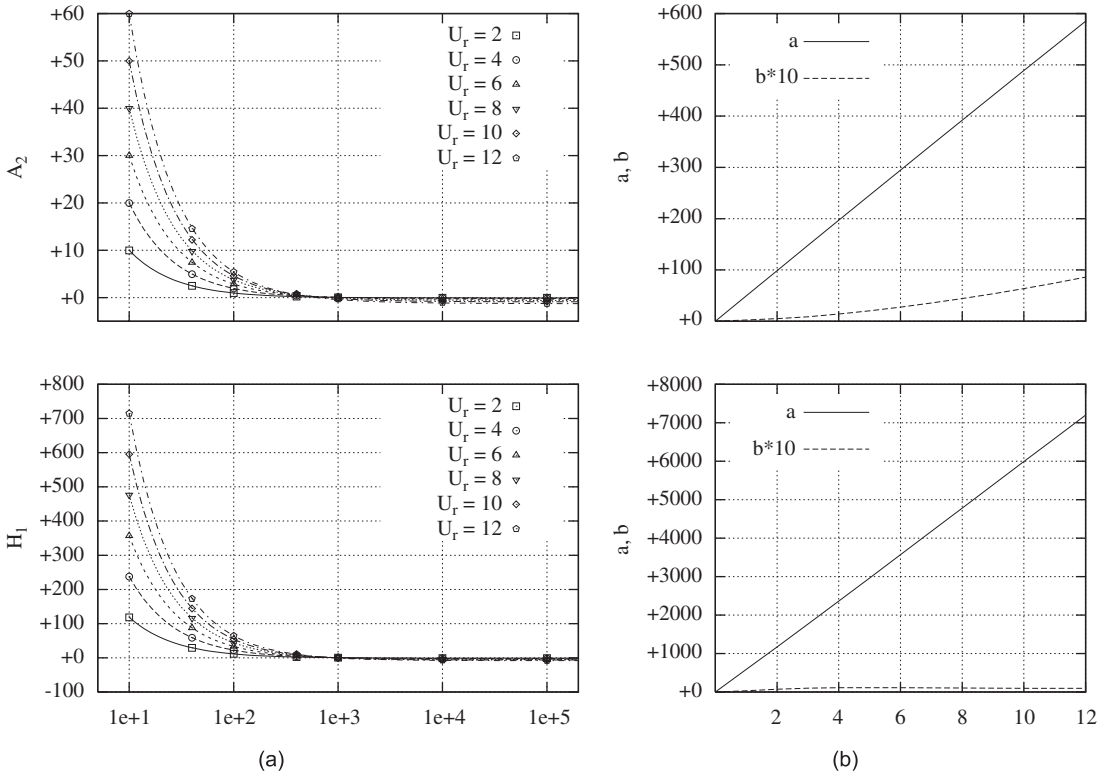

Fig. 18. Flutter derivatives versus Re at given U_r values: one-Re-range fitting.

The proposed approach has been applied to a thick flat plate immersed in a viscous flow. In particular, the Reynolds number effects on flutter derivatives are investigated in a wide range of Re. The computational approach permits an easy visualization and points out some motion-induced fluid flow phenomena during the post-processing stage. For each flow phenomenon, a representative quantity is selected and its dependency on the Reynolds number is recognized. A combination of these Reynolds number dependencies can also be recognized in the flutter derivatives. In particular, H_1 and A_2 are mainly affected by inertial and viscous in-motion forces. The significant Re effects on all the derivatives for $\mathrm{Re} \leqslant 10^5$, and especially on H_1 and A_2, would suggest not using the closed-form solution in real low Re flows. The same Re effects are expected to still hold in bluff body aeroelasticity, even though other Re effects can take place on boundary layer separation.

Acknowledgements

The authors wish to express their grateful thanks to the L3M-Laboratoire de Modélisation et Simulation Numérique en Mécanique, Marseille, France for kindly making their computing facilities available. Thanks are also due to the OptiFlow Company for its support.

References

Batina, J., 1989. Unsteady Euler airfoil solutions using unstructured dynamic meshes. AIAA Paper 89-0115

Brar, P., Raul, R., Scanlan, R., 1996. Numerical calculation of flutter derivatives via indicial functions. Journal of Fluids and Structures 10, 337–351.

Dickinson, M., Gotz, K.G., 1993. Unsteady aerodynamic performance of model wings at low Reynolds number. Journal of Experimental Biology 174, 45–64.

Donea, J., 1996. An arbitrary Lagrangian–Eulerian finite element method for transient fluid–structure interactions. Computational Methods in Applied Mechanical Engineering 33, 689–723.

Eymard, R., Gallouët, T., Herbin, R., 2000. Finite volume methods. In: Handbook of Numerical Analysis, vol. VII. North-Holland, Amsterdam.

Ferziger, J.H., Peric, M., 2002. Computational Methods for Fluid Dynamics, third ed. Springer, Berlin.

Fransos, D., Bruno, L., 2006. Determination of the aeroelastic transfer functions for streamlined bodies by means of a Navier–Stokes solver. Mathematical and Computer Modelling 43, 506–529.

Fung, Y., 1993. An Introduction to the Theory of Aeroelasticity. Dover, New York.

Garrick, I., 1938. On some reciprocal relations in the theory of nonstationary flows. NACA Technical Report 629.

Halfman, R., 1952. Experimental aerodynamic derivatives of a sinusoidally oscillating airfoil in two dimensional flow. NACA Technical Report 1108.

Jeong, U., Kwon, S., 2003. Sequential numerical procedures for predicting flutter velocity of bridge sections. Journal of Wind Engineering and Industrial Aerodynamics 91, 291–305.

Khris, S., 1998. Contribution de modèles de turbulence du premier ordre à la simulation numérique d'écoulements aérodynamiques en situation hors-équilibre. Ph.D. Thesis, Université de la Mediterranée, Aix Marseille II, Marseille.

Le-Maître, O.P., Scanlan, R.H., Knio, O.M., 2003. Estimation of the flutter derivatives of an naca airfoil by means of Navier–Stokes simulation. Journal of Fluids and Structures 17, 1–28.

Lesieutre, D., Reisenthel, P., Dillenius, M., 1994. A practical approach for calculating aerodynamic indicial functions with a Navier–Stokes solver. AIAA Paper 94-0059.

Matsumoto, M., 1996. Aerodynamic damping of prisms. Journal of Wind Engineering and Industrial Aerodynamics 59, 159–175.

Nomura, T., Hughes, T., 1992. An arbitrary Lagrangian–Eulerian finite element method for interaction of fluid and a rigid body. Computational Methods in Applied Mechanical Engineering 95, 115–138.

Scanlan, R.H., Tomko, J.J., 1971. Airfoil and bridge deck flutter derivatives. Journal of Engineering Mechanics Division 97 (6), 1717–1737.

Schaaf, S., Sherman, F., 1954. Skin friction in slip flow. Journal of Aeronautical Sciences 21, 85–90.

Schlichting, H., 1979. Boundary-Layer Theory, seventh ed. McGraw-Hill, New York.

Simiu, E., Scanlan, R., 1996. Wind Effects on Structures: Fundamentals and Applications to Design. Wiley, New York.

Sun, Q., Boyd, I.D., 2004. Flat-plate aerodynamics at very low Reynolds number. Journal of Fluid Mechanics 502, 199–206.

Sunada, S., Sakaguchi, A., Kawachi, K., 1997. Airfoil section characteristics at a low Reynolds number. ASME Journal of Fluids Engineering 119, 129–135.

Theodorsen, T., 1935. General theory of aerodynamic instability and the mechanism of flutter. NACA Technical Report 496.

Vairo, G., 2003. A numerical model for wind loads simulation on long-span bridges. Simulation Modelling Practice and Theory 11, 315–351.

Walther, J., Larsen, A., 1997. Two dimensional discrete vortex method for application to bluff body aerodynamics. Journal of Wind Engineering and Industrial Aerodynamics 67/68, 183–193.